Investigating the Role of Fluid Dynamics and Wall Mechanics in Atherosclerosis, Plaque Rupture, and Plaque Excavation in the Human Carotid Bifurcation

Scott T. Lovald, Tariq Khraishi, Juan Heinrich
Mechanical Engineering Dept., University of New Mexico

Howard Yonas, Christopher Taylor
Dept. of Neurosurgery, University of New Mexico

Abstract

Atherosclerosis affects millions of people worldwide and can lead to heart attack and stroke. The human carotid artery bifurcation is a critical site often affected by plaque and atherosclerotic formations. Over time, atherosclerosis can grow from mild to severe depending on both mechanical and biological responses in the artery wall. A computational fluid dynamics model of the human carotid bifurcation with fluid structure interaction has been created to explore the nature of atherogenesis, plaque excavation and plaque rupture. Artery geometry, plaque geometry and boundary conditions were based on magnetic resonance imaging scans and spectral Doppler ultrasound scans obtained from patients at the University of New Mexico Hospital. In the current study, results for fluid velocity and wall shear stress corroborate results of previous studies that the region of plaque stenosis is characterized by low flow velocities, reversed flow, strong secondary flows and low wall shear stress. Fluid structure interaction results of the model support theories that these regions are further characterized by high arterial wall strain.

Introduction

Atherosclerosis affects millions of people worldwide and can lead to heart attack and strokes. Strokes kill about 150,000 Americans each year as the third leading cause of death behind heart disease and cancer[8]. The human carotid artery bifurcation is a critical site often affected by plaque and atherosclerotic formations. Atherosclerosis is prone to develop in areas of flow disruption such as the carotid artery bifurcation, coronary arteries, and the abdominal aorta[8].

The left and right carotid arteries are the main vessel to send oxygen rich blood to the head and brain. Exiting the aortic arch, each common carotid artery runs through the neck and branches into two sections. The larger internal carotid artery supplies blood directly to the brain while the smaller external carotid artery and its branches supply blood to other areas in the head and face. A stroke occurs when blood flow to the brain is diminished or stopped.

Atherosclerosis increases the chance of stroke in three ways[3]:

1. Narrowing of the artery (stenosis) through plaque build up on the artery walls. A high degree of stenosis due to plaque deposit in the carotid artery can significantly diminish blood flow to the brain[5].
2. A blood clot, or thrombus, will become lodged in a narrowed artery and block the flow of blood to the brain.
3. Plaque will break away from the original formation and become lodged in a smaller artery downstream, again blocking the flow of blood.

For three decades, local flow anomalies such as flow separation, recirculation, low wall shear stress, and high local particle residence time are factors that have been implicated in the development of arterial diseases[5,6]. Atherosclerosis is a chronic inflammatory response in the walls of the artery[1]. Plaque growth is due in large part to the deposition of lipoproteins related to cholesterol levels. Over time, atherosclerosis can grow from mild to severe depending on both mechanical and biological responses in the artery wall. Given the localization of inflammation to bifurcated regions, fluid dynamics and wall mechanics are proposed to have a large effect on this process. Numerical analysis of flow through a stenotic carotid bifurcation provides insight into local flow dynamics and an assessment of the risks of particular modes and degrees of stenosis.

Further danger of plaque deposit is that ruptured particles can be carried off to the brain and lead to a stroke[9]. One such phenomenon of plaque rupture, plaque excavation, is observed clinically as blood flow tunneling through the embolism at high degrees of stenosis. Numerical analysis allows the examination of vessel pressure and wall shear stress distributions to gather insight into probable locations and modes of plaque rupture. Both qualitative and quantitative results from numerical analyses provide surgeons and vascular physicians with further means to mitigate these risks.

A computational fluid dynamics (CFD) model of the human carotid bifurcation with fluid structure interaction (FSI) has been created to explore the nature of atherogenesis, plaque excavation, and plaque rupture. The fluid will be modeled as transient Newtonian blood flow. These flow conditions are determined using Doppler ultrasound scans taken from a patient at the University of New Mexico Hospital (UNMH). The arterial wall will be modeled as nonlinear hyperelastic according to the Mooney-Rivlin model. The model will explore measures of arterial wall pressure, wall shear stress, wall shear stress gradient, and the oscillatory shear index at different degrees of atherosclerotic stenosis. The form of the plaque is determined using CT scans of a patient with moderate plaque stenosis at UNMH. This is the first model that considers a growing plaque to determine the evolution of pertinent pressure and stress measures from mild to severe stenosis as well as the first known exploration of plaque excavation.

Perktold[6] performed a study using computer simulation of pulsatile, non-Newtonian flow in both rigid and compliant carotid artery models. The first part of the study focused on determining the effect of bifurcation geometry on the flow and stress fields in the artery. The two bifurcation models considered were a wide angle carotid with relatively narrow sinus diameter and an acute angle carotid with an enlarged sinus diameter. During systolic deceleration, both models show separation and recirculation at the outer wall, while the acute model also showed recirculation on the divider wall. Flow separation in the wide angle model starts at the transition between the common carotid and the internal carotid and extends into the internal carotid. Flow separation in the acute angle carotid starts well within the common carotid and extends only to the beginning of the internal carotid. This observation is correlated with atherosclerotic plaque locations in patients. Wide angled arteries are seen to have plaque develop in the sinus while acute angled arteries are observed to have plaque develop near the transition between the common carotid and the internal carotid.

The second part of the study compared the rigid wall model to a distensible wall model. The wall material was modeled using Young's modulus data from maximum local displacement data. The distensible wall model was seen to reduce the flow velocities as well as decrease flow separation and recirculation during systolic deceleration. Overall, wall shear stress magnitude was lower in the distensible model.

Perktold[7] performed another study on the effect of distensible wall models on quantitative numerical results. This time more focus was given to the stresses within the arterial wall. The model used pulsatile non-Newtonian flow with a shear thinning model. The wall was modeled using a thin shell structure with large deformation capabilities, as expected displacements were to exceed 10-12%. Again the material model for the wall assumed elastic and isotropic behavior with the elastic modulus and Poisson's ratio based on experimental displacement data and corresponding pressure data. The ends of the arterial walls were constrained from movement in all directions. The geometry of both the rigid and distensible models was idealized with the angles between each of the internal and external carotids and the common carotid measuring 25 degrees.

General results showed strongly skewed velocity profiles with the highest velocities near the divider walls in both the internal and external carotid arteries. Reversed flow was found on the outer sinus wall at systolic flow deceleration and during systolic minimum flow rate. Compared to the rigid model, the distensible model showed less maximum reversed flow at the max sinus diameter cross section during systolic deceleration, at systolic minimum, and during the minimum flow rate. High shear stress was found on the internal carotid inner divider wall while low shear stress was found the corresponding outer wall. For high values of shear stress, the distensible wall model had values that were up to 25% lower than those of the rigid wall model.

Zhao[11] created a numerical model of the human carotid bifurcation using geometry from magnetic resonance imaging and boundary conditions using Doppler ultrasound and applanation tonometry. The fluid structure interaction of the arterial wall was modeled using a shell model with the material being incrementally linear elastic. The elastic modulus of the wall is E= 2.6 x 10^5 N/m^2 and the wall thickness of 0.4 to 0.66 mm was determined using M-mode measurements and B-mode ultrasound, respectively. The model was solved using an iterative coupled algorithm with the equations of motion of the flow and the wall movement solved simultaneously.

General flow characteristics show skewed velocity profiles near the divider wall due to the branching of the bifurcation arteries. Strong asymmetric secondary flow was once again found in the bulb area. The slow flow zone extends into the common carotid during the more disturbed decelerated flow. There is a significant overlap between high wall mechanical stress zones and low wall shear stress zones near the bulb. This leads to speculation on this combination of factors leading to lesion development. Compared to a rigid wall model, the distensible model is seen to have a larger slow moving zone and smaller wall shear stress values over much of the artery. Decreased wall shear stress is especially apparent during peak systole, agreeing with the intuitive notion that an expandable artery will increase its cross sectional area and consequently decrease the velocity of the flow field contained within. Comparison to experimental results show good correlation with calculated wall movement and demonstrate that wall displacement is likely driven by the inlet pressure waveform.

The study reinforces the belief that wall shear stresses have an influence on biological changes in the wall. As high tensile stresses have been linked to vessel wall thickening and alternations in composition, the combination of low wall shear stress and high mechanical stress in areas prone to plaque initiation is an important observation.

Younis[11] used finite element simulation studied the inter-individual variations in flow dynamics and wall mechanics in the carotid artery bifurcation. CFD models for three healthy volunteers were obtained using MRI for geometry and ultrasound for the boundary conditions. Blood was assumed incompressible, Newtonian, and laminar; considered a reasonable assumption for large arteries. Flow rates were applied at the common and internal carotid inlet and outlet while the rate at the external carotid was calculated as the difference between the two to ensure conservation of mass. The arterial wall was modeled as nearly incompressible using a hyperelastic model including large strain and displacement. The original model geometry was shrunk by 10% to simulate the ex-vivo state before being subjected to an axial pre-stretch of 10%.

Results in all three patients show the carotid bulb to have low wall shear stress values relative to other regions of the model and flow separation on its non-divider wall. Flow separation is greatest during the decelerative phase of systole. High wall shear stress temporal gradient and high cyclic strain are shown in the carotid apex at the transition in the outer wall of the common carotid and external carotid junction. Early atherosclerotic inflammation is commonly observed in these areas. High wall shear stress temporal gradient is associated with expression of atherogenetic genes in endothelial cells while cyclic strain is associated with the stimulation of endothelial and smooth muscle cells. Circumferential variations in cyclic strain are observed in the models and in ultrasound measurements of the healthy volunteers. It was further determined that while stress and strain magnitude was affected by the inclusion of residual stress, the cyclic strain amplitude remains relatively unchanged. It has previously been determined that endothelial cells adapt only to dynamic strain levels and are not responsive to mean strain levels. The results of this study ultimately support the theory that atherosclerosis is multi-factorial.

Methods

CFD Model Geometry Creation

A 3-dimensional finite element model of the human carotid bifurcation was created in ANSYS 8.0. The geometry of the carotid bifurcation was determined using common measurements put forward by Gijsen[4] (Fig. 1). Primitives in the ANSYS preprocessor were created to approximate this geometry for the common carotid, internal carotid, sinus, and external carotid. Boolean operations were performed to intersect the primitives and form the continuous bifurcated region. Figure 1 shows the geometry of a healthy carotid artery with no simulated plaque stenosis.

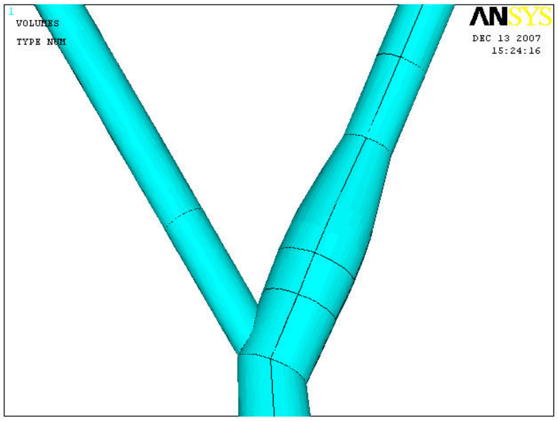

Figure 1. Model geometry for the human carotid artery bifurcation

Two dimensional scans from a 27-year-old patient at the University of New Mexico Hospital were obtained for comparison to the geometrical model. Table 1 shows the results of these measurements and their model counterparts. All measurements within the bulb and the common, internal, and external carotid arteries were determined to be within 10 percent of their corresponding measurements in the ANSYS model. This is considered to be well within inter-patient variability.

Geometry Measurements

	Model (mm)	Scans (mm)	% Difference
Common Carotid Diameter (Proximal)	8.0	7.6	4.8%

Bulb Diameter	8.9	8.1	9.0%
Internal Carotid Diameter (Medial)	5.6	5.1	8.3%
External Carotid Diameter (Proximal)	4.6	4.8	4.8%

Table 1. Diameter measurements for the internal carotid, common carotid, external carotid and the carotid bulb taken from two dimensional CT scans are compared to the corresponding geometrical measurements in the CFD model.

To consider plaque stenosis, the base healthy model is modified. The geometry of plaque stenosis is determined by imaging the carotid arteries of a patient with moderate plaque stenosis. Two dimensional CT scans of the patient were imported into Mimics 8.0. Mimics can create solid 3D entities using segmentation of grayscale values within 2D images. Thresholding functions were used to determine the lumen area of the carotid arteries and create separate solid entities for these arteries. Due to the resolution of the scanner, only the lumen could be imaged, while no useable information could be determined pertaining to the plaque and the arterial wall of the arteries. Figure 2 shows the 3D left and right carotid arteries.

Figure 2. Three dimensional entities were created for the left and right carotid artery bifurcation for a patient with moderate stenosis.

Due to the prevalence of stenosis, the right artery was chosen as the model for the plaque geometry. Using the two dimensional scans the plaque is imaged as an interruption in the lumen. Figure 4 shows a 2D image of the right artery in the sagittal plane. Interpolating the boundary of a healthy artery, measurements were taken for the "error" of the actual lumen against its interpolated boundary (Fig. 4). These measurements give the approximate form of the plaque stenosis.

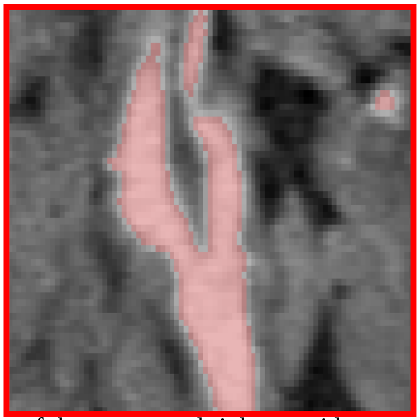

Figure 3. Two dimensional scan of the segmented right carotid artery. The plaque stenosis is imaged as an interruption in the lumen.

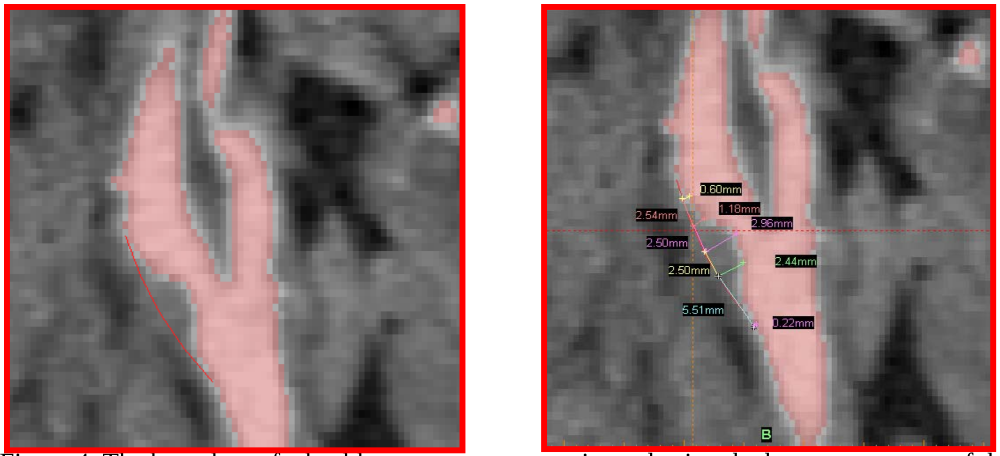

Figure 4. The boundary of a healthy artery was approximated using the known geometry of the lumen. Linear measurements were taken for the difference between the healthy and diseased arteries to discover the approximate form of the plaque.

A modified geometry of the ANSYS model was created using the “error” scheme determined from the Mimics measurements. A scalar multiplier was used to modify the plaque geometry sufficiently to approximate different degrees of plaque stenosis according to the NASCET standard. The creation of the model in this manner allows the parametric study of the sole effect of plaque growth through the use of the scalar multiplier while keeping all other model parameters consistent. Figure 5 shows lines approximating the healthy artery and lines approximated the form of the plaque growth within the artery. Cross sections based on these lines were created and arterial volumes were created using a bottom-up approach by skinning areas across the irregular cross sections.

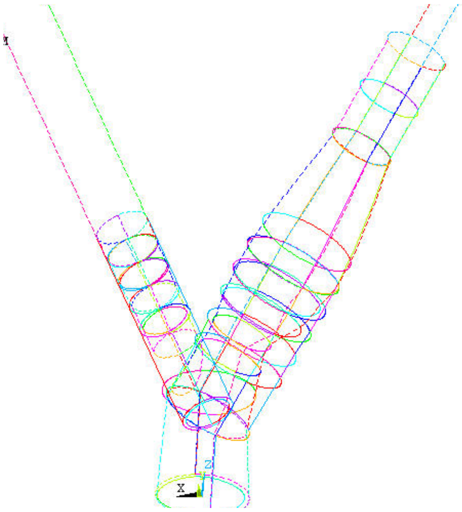

Figure 5. Geometrical lines showing the approximation of the plaque form for growth within the healthy carotid artery.

The model was meshed using Fluid 142 3D elements. In the common, internal and external arteries away from the bifurcation a structured mesh was used to minimize computational time and encourage solution convergence. Due to the complicated geometry, an unstructured mesh was used in the bifurcation region including the carotid sinus. Figure 6 shows the meshed model geometry for a healthy artery with no stenosis and an artery suffering stenosis of 80% NASCET.

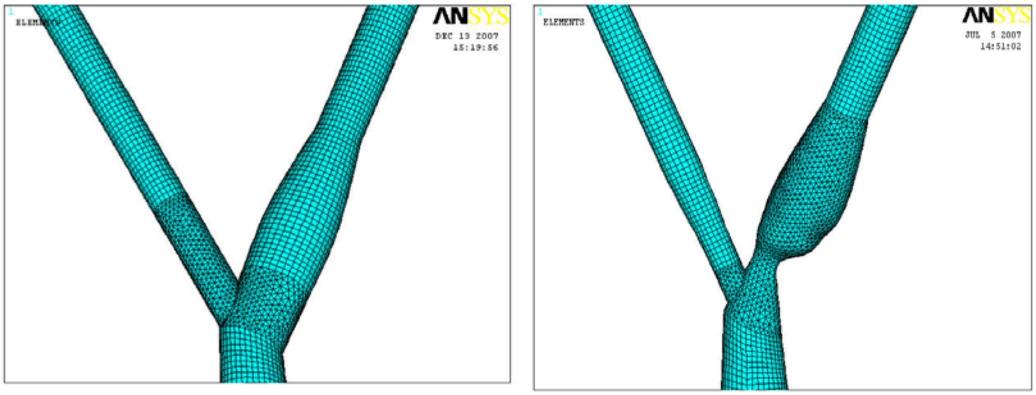

Figure 6. Meshed bifurcation models for a carotid with no stenosis and a carotid simulating 80% stenosis according to NASCET.

Flow Conditions

The blood flow is assumed to be incompressible and Newtonian with properties for dynamic viscosity of 0.0035 Pa*s and a mass density of 1060 (kg/m^3)[4]. The blood flow is pulsatile in nature and is modeled using a transient flow scheme. Although abundant information can be found in the literature, validation of commonly used boundary conditions was required to ensure model accuracy. Spectral Doppler Ultrasound scans were taken from a healthy 27-year-old male patient in the region of the internal carotid artery. Figure 7 shows the velocity contours and the pulse waveform in the distal internal carotid artery. Values for the peak velocity in the artery were determined for the entire pulse period and are given in Figure 8. The values were also compared to mass flow conditions used by Zhao[12]. The comparison shows less than a 10% difference in peak internal carotid velocities.

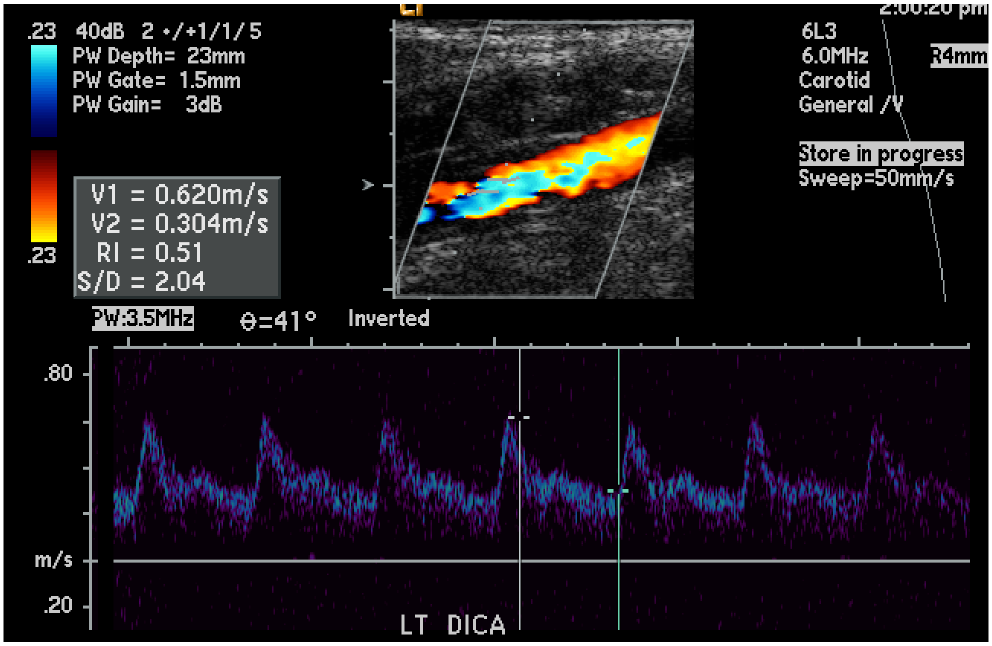

Figure 7. Doppler ultrasound scan of the velocity flow waveform in the distal internal carotid artery of a healthy patient.

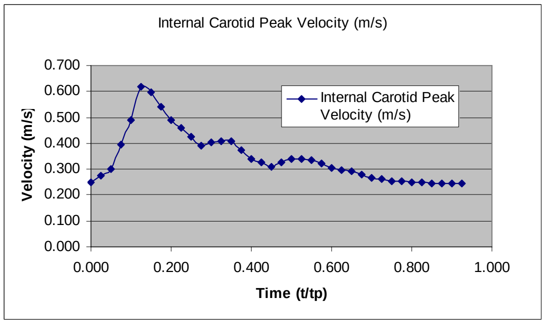

Peak Velocity Measurements

		Model (m/s)	Scans (m/s)	% Difference
Internal Carotid Artery (Medial)	Systole	0.66	0.62	6.5%
	Diastole	0.34	0.30	9.8%

Figure 8. Peak velocity boundary conditions in the internal carotid artery. The velocity in the internal artery was compared to published values given in Zhao[12].

Due to flow rate similarities, the common carotid pressure and the external carotid flow rate were obtained from Zhao[12]. Fully developed flow was assumed at the internal and external artery outlet, while the outlet was a sufficient distance downstream from the bifurcation and carotid sinus to ensure that boundary condition assumptions would not have an effect on pertinent result data. Figure 9 shows all data used for the transient flow conditions.

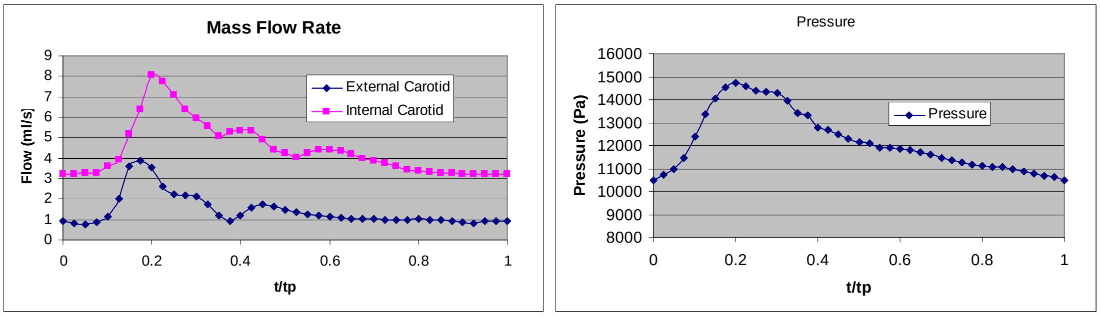

Figure 9. Velocity and pressure boundary conditions used in the current study.

The pulse period was implemented in 40 time steps. The number of substeps for each time step is dependent on the velocity gradient near that step and was determined based on monitoring solution convergence. The total pulse period was broken into four stages to facilitate substep convergence (see Fig. 10). Sectioning of the period was estimated according to the severity of the input gradient. The number of substeps was increased for each step within each stage until pertinent results measures showed less than a 1 percent change over the previous run (Fig. 11). The number of substeps was determined for each stage as the following: Stage 1 – 225 steps; Stage 2 – 185 steps; Stage 3 - 45 steps; Stage 4 – 40 steps.

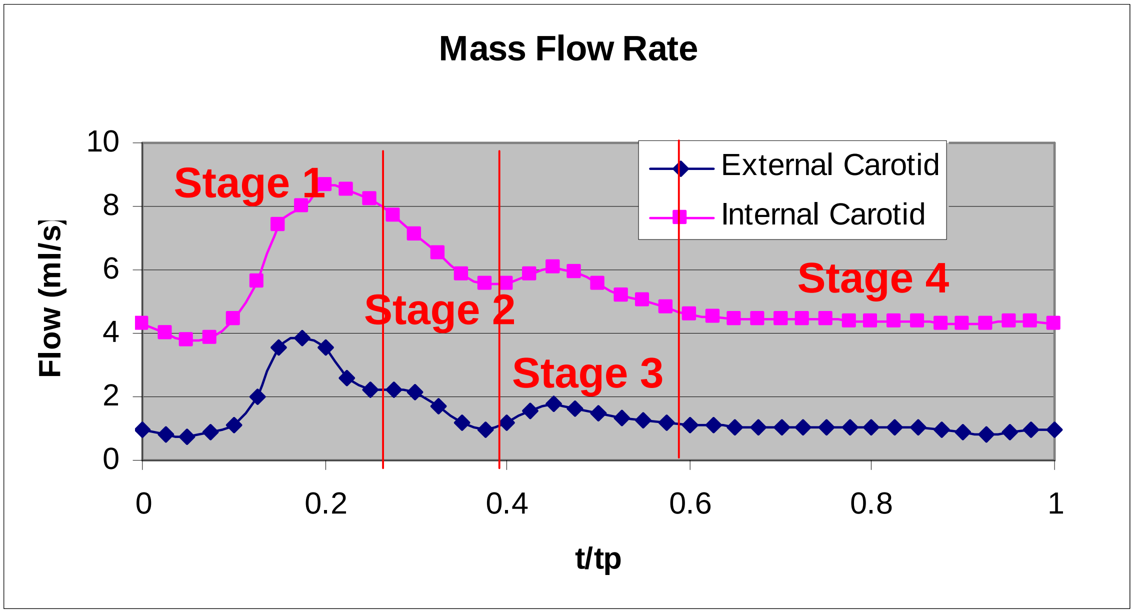

Figure 10. The entire cardiac period was broken into 40 time steps. The number of substeps per time step is determined by breaking the period into four stages and increasing the number of substeps until results had sufficiently converged.

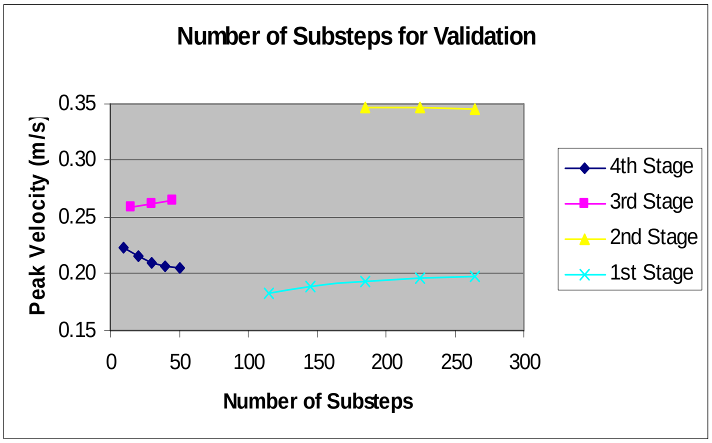

Figure 11. Peak velocity in the carotid sinus for a time step in each stage of the cardiac pulse as the number of substeps is increased.

To ensure the initial conditions of the transient solution were not affecting the results, the analysis was run through three consecutive periods. Peak pressure and velocity results were taken for all nodes within a cross sectional area within the carotid sinus region. Table 2 gives results that show that periodicity has little effect on these results.

Period	1		2		3	
	Pressure	Velocity	Pressure	Velocity	Pressure	Velocity
Substep 4	12408	0.196	12408	0.197	12408	0.197
Substep 12	14280	0.349	14280	0.349	14280	0.348

Table 2. Peak pressure and velocity results of the carotid model taken at a cross sectional area within the carotid sinus.

Fluid Structure Interaction

The vessel wall is modeled as a 5 parameter Mooney-Rivlin hyperelastic material using Shell 181 elements with a thickness of 2.54 mm. The stress-strain relationship of a hyperelastic material is derived from a strain energy density function (W). Specifically, each stress component is derived as the derivative of *W* with respect to its corresponding strain component. The form of the strain energy potential for the model is given by the following equations:

$$W = c10(\bar{I}1-3) + c01(\bar{I}2-3) + c20(\bar{I}1-3)^2 + c11(\bar{I}1-3)(\bar{I}2-3) + c02(\bar{I}1-3)^2 + \frac{1}{d}(J-1)^2$$

$where$

$\bar{I}_p = J^{-1/3} * I_p : for\_p = 1,2,3$

$c10, c01, c20, c11, c02 = material\_cons\tan ts$

$d = material\_incompressibility\_parameter$

$I_p = in\operatorname{var}aiants\_of\_the\_right\_Cauchy-Green\_deformation\_tensor$

$J = ratio\_of\_the\_deformed\_elastic\_volume\_to\_undeformed\_volume$

The material coefficients are as follows: c10 = -76738690; c01 = 91638354; c20 = 3074221; c11 = -15613094; c02 = 42999974; and d = 0. The parameter values were determined using experimental information from Tang[10]. Figure 12 shows the constitutive behavior of the model overlaid on the experimental data.

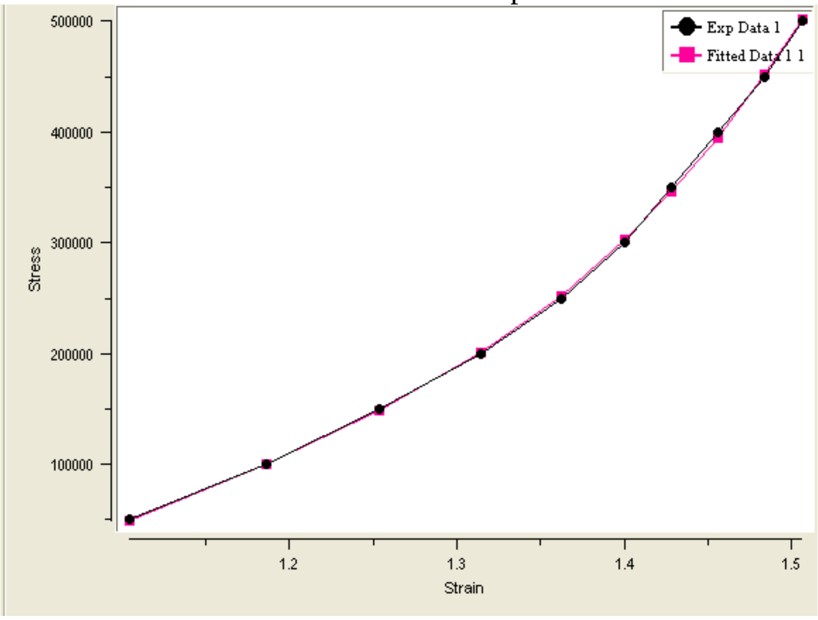

Figure 12. Stress/strain data for the Mooney-Rivlin model compared to experimental data from Tang et al.[10]

Model Validation

The number of elements in the fluid domain is doubled to determine the effect on peak velocity and peak wall shear stress in the internal carotid artery. Doubling elements from 25,560 to 51,440 is shown to change the peak velocity by only 1.24% while the wall shear stress is changed by only 0.06 percent. These results are shown in Table 3.

Mesh Size	**Number of Elements**	**Execution**	**Peak Velocity (m/s)**	**Peak WSS (Pa)**

0.00054	**51,440**	**20 iterations**	**0.144**	**0.000647**
0.00070	**25,560**	**20 iterations**	**0.146**	**0.000647**
		Percent Difference	**1.24%**	**0.06%**

Table 3. Peak velocity and peak wall shear stress for the fluid model with 25,560 elements and 51,440 elements.

Results from the final fluid model are compared to experimental results from Gijsen et al.[4]. The current model has similar geometry and the boundary conditions mimic those of the Gijsen model for the comparison. The difference between the model and the experimental peak velocities at their corresponding cross sections in the internal carotid artery is only 6.44 percent (Table 4).

	Peak Velocity
Current Model	**0.118**
Gijsen	**0.110**
Percent Difference	**6.44%**

Table 4. Peak velocities for the current model and the Gijsen experimental model at corresponding cross sections in the internal carotid artery.

Results

Results are presented for two separate models: (1) a rigid walled model with transient flow conditions and (2) a distensible wall model with steady fluid flow. The steady fluid flow approximates the diastolic flow of the transient flow conditions. Results for the current study consider only the no stenosis case. Results are focused on the fluid velocity and the wall shear stress in the internal carotid artery.

Transient Rigid Walled Model

For the transient model, results are presented at three time steps: t/tp = 0.15, 0.275, and 0.875. These time points represent points within systolic acceleration, systolic deceleration, and diastole, respectively.

Results at t/tp = 0.15

Velocity and pressure contours at t/tp = 0.15 are shown in Figure 13. Generalized flow velocity is at a maximum near the divider wall for both the internal and external carotid arteries. There is a significant amount of flow separation and reversed flow on the outer wall of the internal carotid. Pressure is higher in the internal carotid and the common carotid than the external carotid. Figure 14 shows the outer wall pressure along the length of the common and internal carotid artery. Generally the wall pressure decreases moving from the common to the distal internal carotid artery. There is a sharp decrease in wall pressure near the terminal end of the carotid sinus.

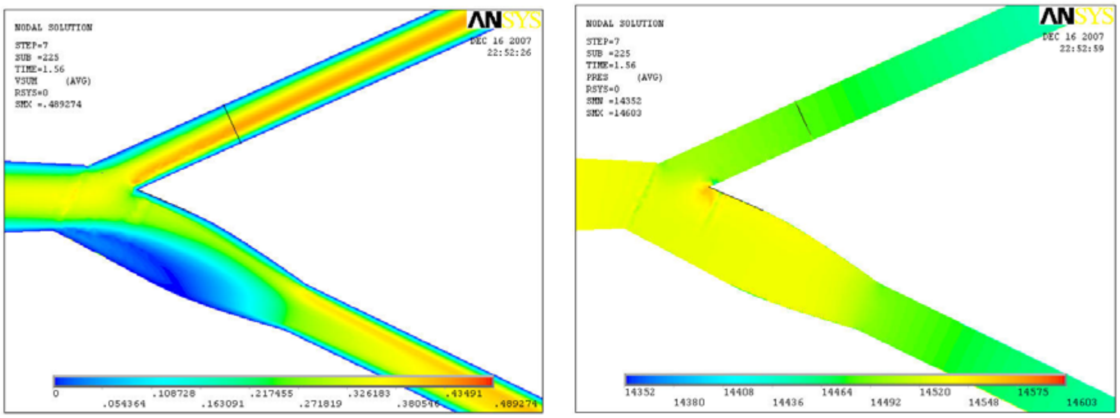

Figure 13. Velocity (m/s) and pressure (Pa) contours at time t/tp = 0.15. Results are shown on the symmetrical plane.

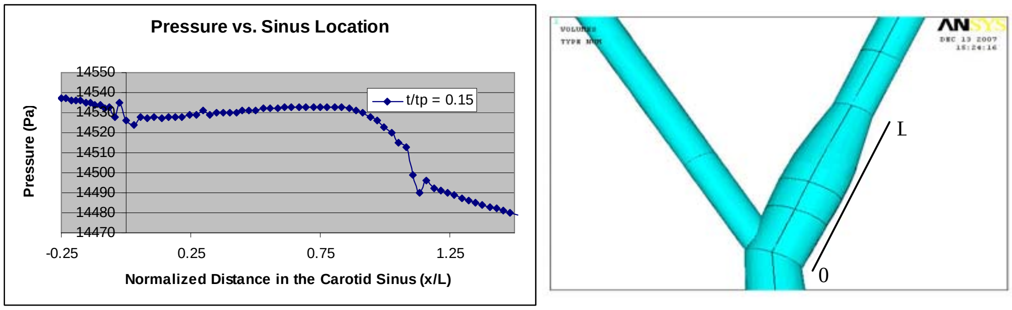

Figure 14. Pressure in the carotid sinus (t/tp = 0.15) along its length from the terminal end of the common carotid to the end of the carotid bulb. The length on the x-axis is defined on the right.

Figure 15 shows velocity vectors on the symmetrical plane during systolic acceleration. The vectors describe very slow flow on the outer wall of the internal carotid artery and very strong reversed flow near the entrance of the internal carotid artery. Figure 16 shows velocity profiles on a horizontal cross section in the internal carotid artery during systolic acceleration. The figure describes strong secondary that accompany the reversed flow vectors.

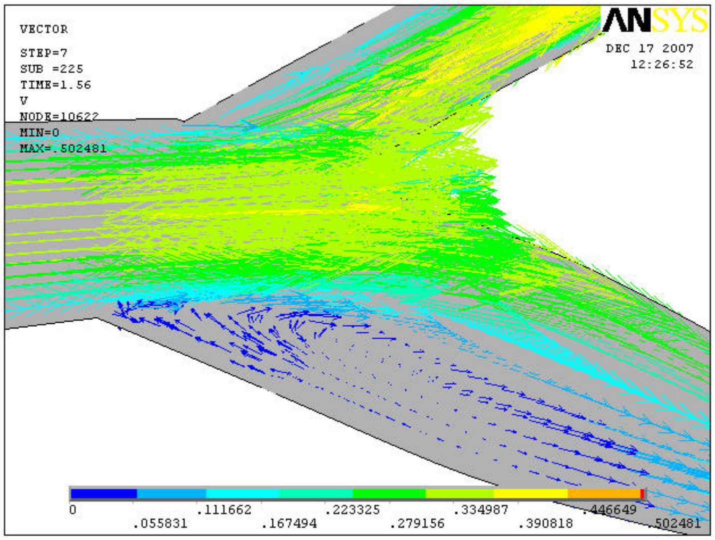

Figure 15. Velocity vectors (m/s) in the artery bifurcation on the symmetrical plane during systolic acceleration.

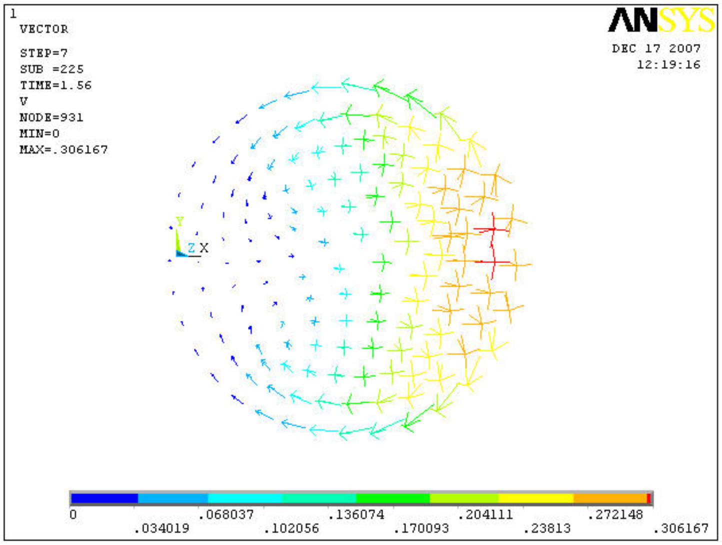

Figure 16. Velocity vectors (m/s) over a cross section in the carotid sinus during systolic acceleration.

Results at t/tp = 0.275

Velocity and pressure contours at t/tp = 0.275 are shown in Figure 17. The general velocity and pressure observations for t/tp = 0.275 are similar to those of t/tp = 0.150. There is both stronger relative velocity flow and a larger region of flow separation and reversed flow during this systolic deceleration phase. Flow field pressure is quantitatively similar for the internal and external carotid arteries. Figure 18 shows the outer wall pressure along the length of the common and internal carotid artery at this time step.

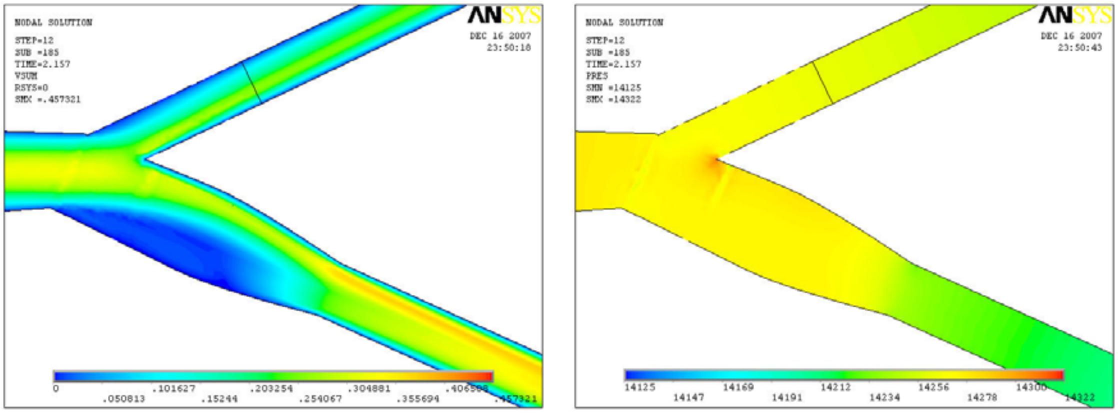

Figure 17. Velocity (m/s) and pressure (Pa) contours at time t/tp = 0.275. Results are shown on the symmetrical plane.

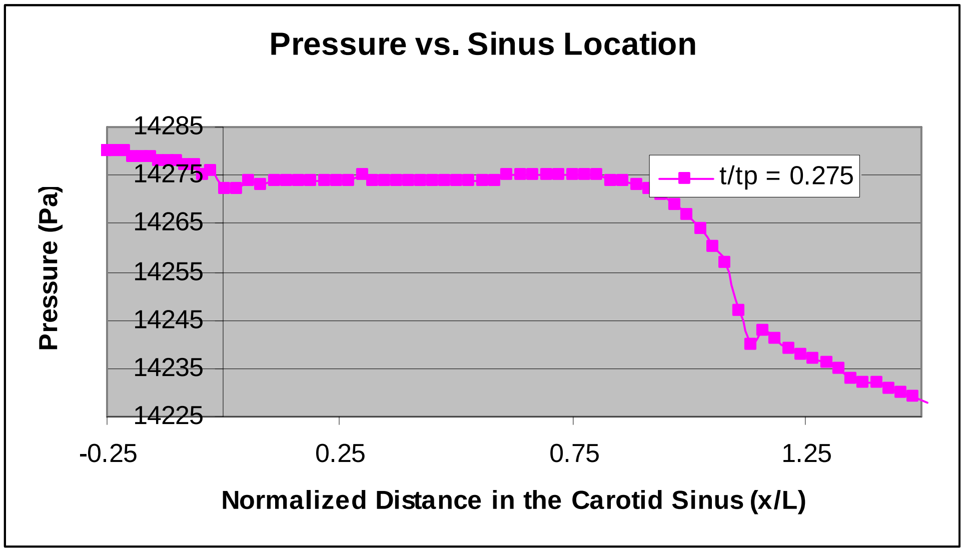

Figure 18. Pressure in the carotid sinus (t/tp = 0.275) along its length from the terminal end of the common carotid to the end of the carotid bulb.

Figure 19 shows velocity vectors on the symmetrical plane during systolic deceleration. Similar to systolic acceleration the vectors describe very slow flow on the outer wall of the internal carotid artery and very strong reversed flow near the entrance of the internal carotid artery. Compared to systolic acceleration, systolic deceleration vectors describe a much larger region of low flow with smaller magnitudes of reversed flow. Figure 20 shows that secondary flows are less pronounced than those of systolic acceleration.

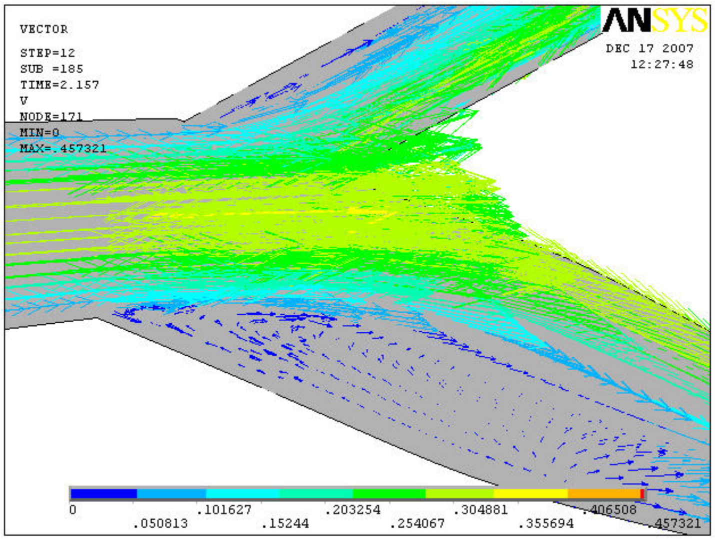

Figure 19. Velocity vectors (m/s) in the artery bifurcation on the symmetrical plane during systolic deceleration.

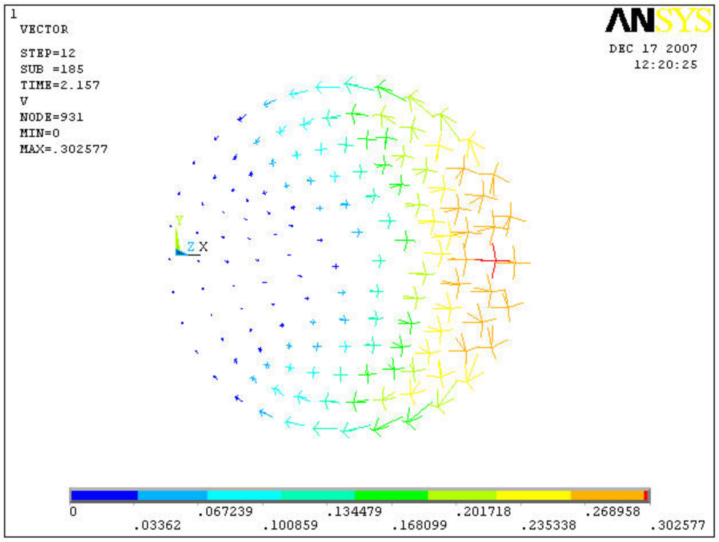

Figure 20. Velocity vectors (m/s) over a cross section in the carotid sinus during systolic deceleration.

Results at t/tp = 0.875

Velocity and pressure contours at t/tp = 0.875 are shown in Figure 21. General flow velocity and pressure fields are very similar for t/tp = 0.875 as in t/tp = 0.275. Figure 22 shows the outer wall pressure along the length of the common and internal carotid artery at this time step. Diastole does exhibit a significant drop in magnitude of velocity and pressure compared to systolic flow fields.

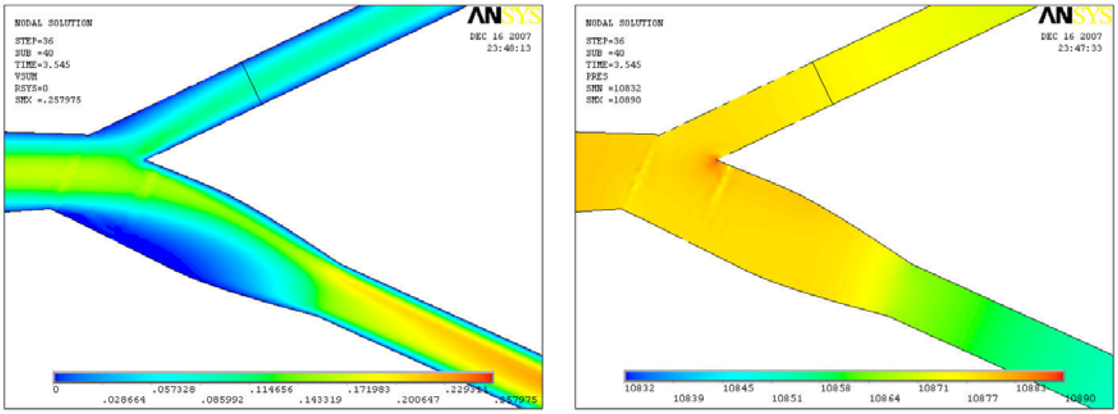

Figure 21. Velocity (m/s) and pressure (Pa) contours at time t/tp = 0.875. Results are shown on the symmetrical plane.

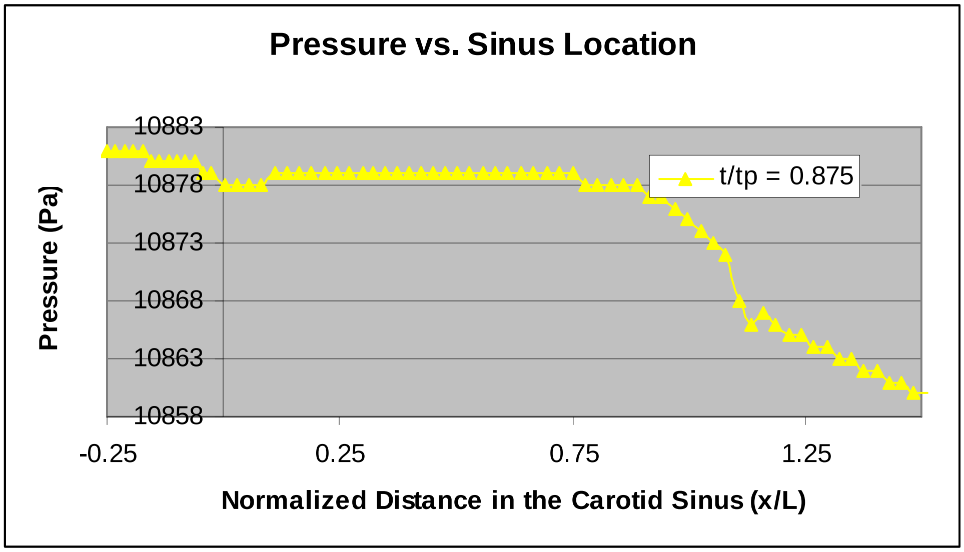

Figure 22. Pressure in the carotid sinus (t/tp = 0.875) along its length from the terminal end of the common carotid to the end of the carotid bulb.

Figure 23 shows velocity vectors on the symmetrical plane during diastole. There is low flow again near the outer wall of the internal carotid but there is little reversed flow compared to the systolic flow. Figure 24 shows velocity profiles on a horizontal cross section in the internal carotid artery during diastole. There is less secondary flow in this flow field when compared to the systolic fields.

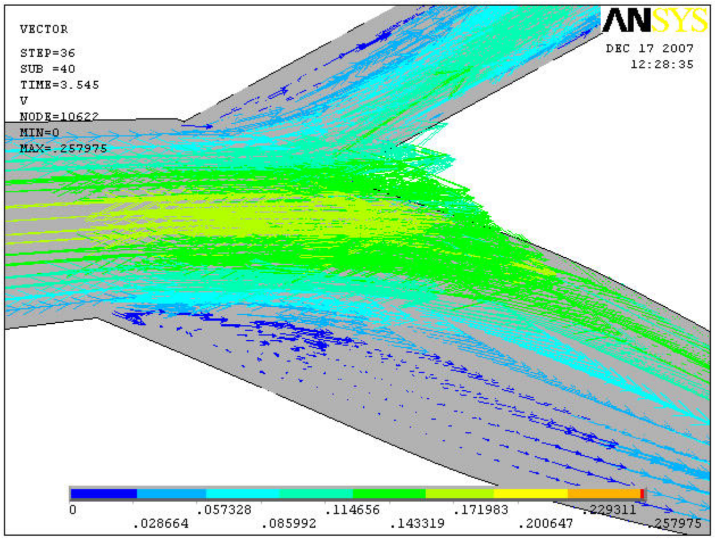

Figure 23. Velocity vectors (m/s) in the artery bifurcation on the symmetrical plane during diastole.

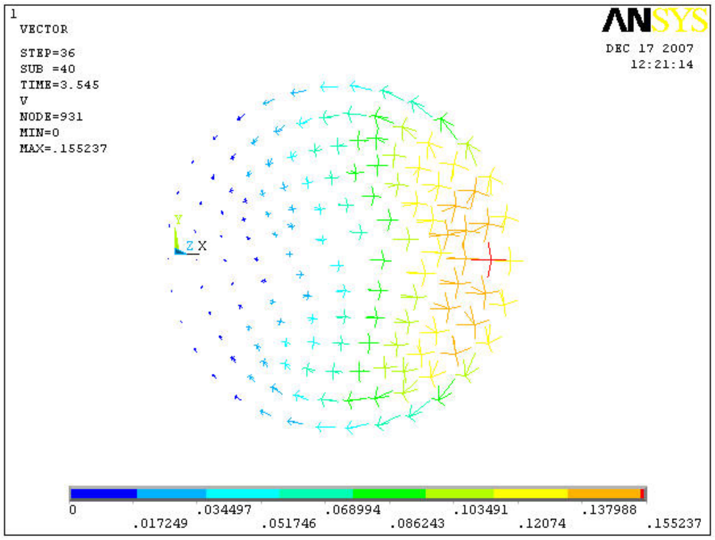

Figure 24. Velocity vectors (m/s) over a cross section in the carotid sinus during diastole.

Figure 25 shows the wall shear stress along the length of the common and internal carotid artery at time steps t/tp = 0.15, 0.275, and 0.875. The figure describes significantly diminished magnitudes of stress in the carotid sinus.

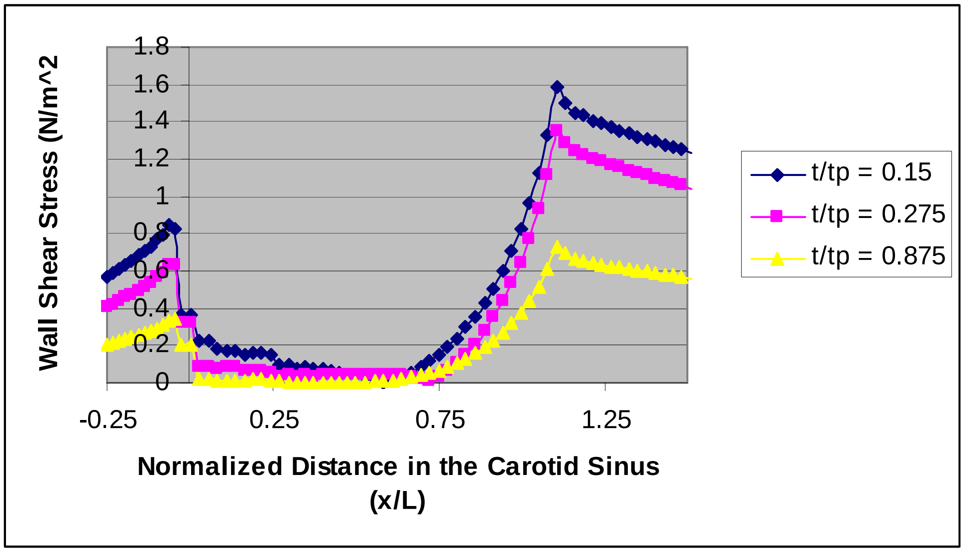

Figure 25. Wall shear stress (Pa) in the carotid sinus along its length from the terminal end of the common carotid to the end of the carotid bulb.

Steady Distensible Walled Model

The second part of the study used a coupled iterative algorithm to solve a fluid structure interaction model of the distensible carotid artery bifurcation. The fluid problem is solved first to determine the fluid pressure boundary conditions applied to the distensible wall. Ten stagger iterations were used to loop through the fluid and solid analyses until convergence is reached. The steady flow approximated the diastolic boundary conditions of the transient model.

Figure 26 shows the top view 1st principal strain in the carotid artery bifurcation during diastole. The view describes significantly higher mechanical strain in the internal carotid compared to the external carotid. The highest strains are seen near the bifurcation region. Figure 27 shows the side view of the 1st principal strain in the artery. The view confirms the symmetry of the strain in the symmetrical plane.

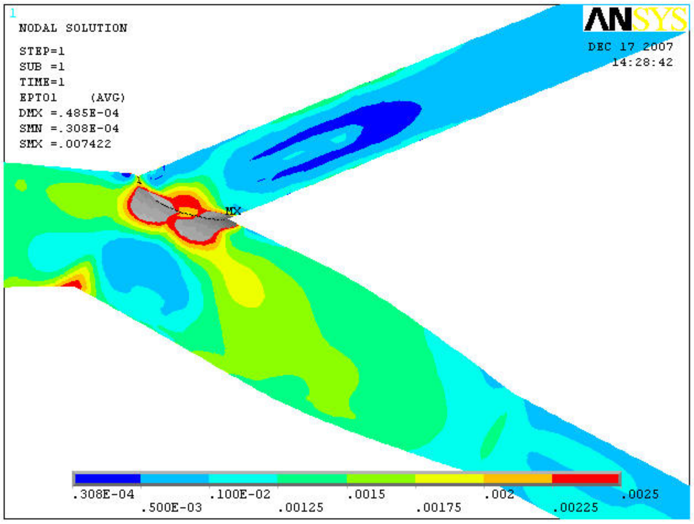

Figure 26. Top view of the 1st principal strain in the carotid artery bifurcation during diastole

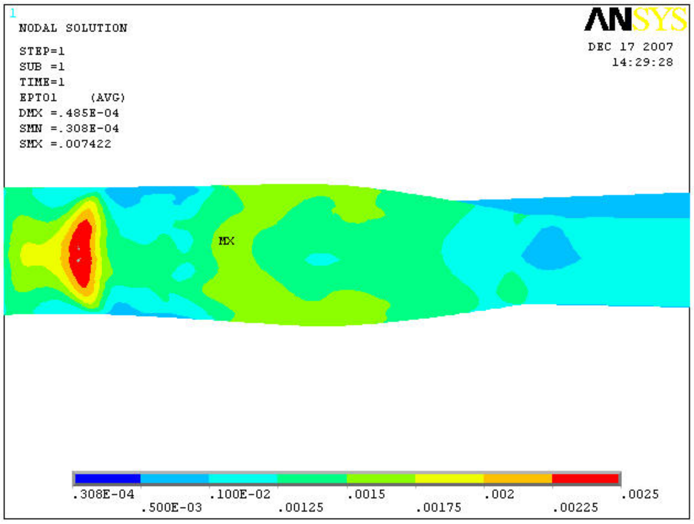

Figure 27. Side view of the 1st principal strain in the carotid artery bifurcation during diastole

Figure 28 shows the wall shear stress on the outer wall of the internal carotid in both the distensible and rigid models with similar flow conditions. The figure describes differing values for both of the models with the greatest difference near the middle of the carotid sinus. At this point the distensible model has as little as half the strain of the rigid model.

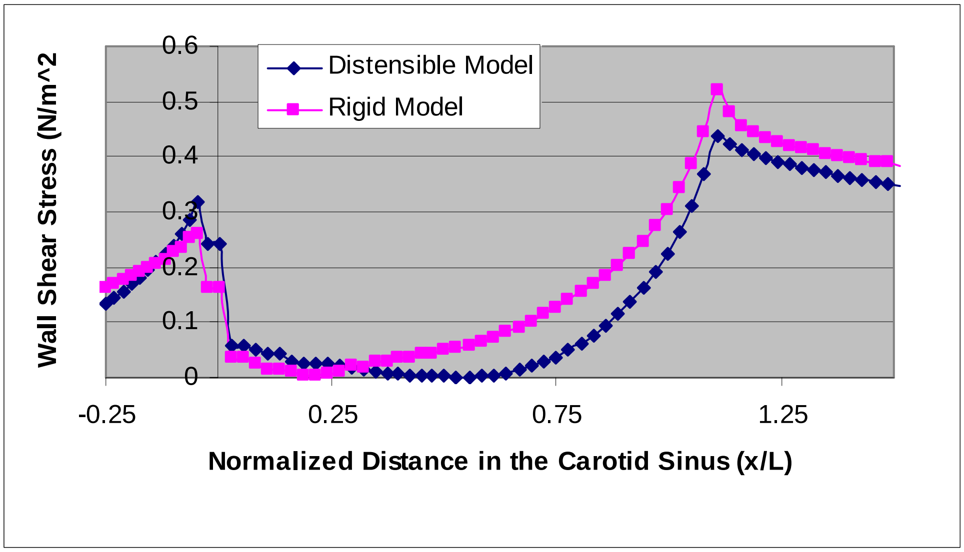

Figure 28. Wall shear stress (Pa) in the carotid sinus along its length from the terminal end of the common carotid to the end of the carotid bulb. Results are shown for the distensible model and a rigid model with the same boundary conditions.

Discussion

A model has been created that can analyze the fluid dynamics and wall mechanics for healthy and diseased carotid artery bifurcations. General results are in agreement with previous findings. Flow velocity profiles are heavily skewed towards the divider walls in both branches while the outer wall of the carotid bulb has significantly diminished flow velocities along with secondary and reversed flows. Atherosclerotic lesions have previously been hypothesized to develop in areas of low wall shear stress[5,6]. The results of the current study reinforce this theory as the junction of the common carotid and internal carotid along with the carotid bulb have relatively small strain rates in comparison to the rest of the artery.

Similar to findings by Perktold[7] the distensible model was seen to reduce the magnitude of wall shear stress up to 30% at relatively high stress areas. 1st principal strain was seen to be relatively high at the transition between the common carotid and the internal carotid, similar to observations by Younis et al.[11]. The results of this steady fully support the theory that high mechanical strain and low wall shear stress multifactorially have a positive effect on the inflammatory response of the arterial wall.

Future work will include implementing transient flow conditions upon the distensible wall model. It is expected this will be required be the differences between rigid and distensible models can fully be appreciated. Upon validation of the transient distensible model differing levels of carotid stenosis will be implemented to fully analyze the plaque excavation phenomenon.

References

1. "Atherosclerosis" www.wikipedia.org
2. Baaijens, J.P.W., Van Steenhoven, A.A., and Janssen, J.D., 1993, "Numerical Analysis of Steady Generalized Newtonian Blood Flow in a 2D Model of the Carotid Artery Bifurcation," Biorheology, Vol. 30, pp. 63-74.
3. "Carotid Artery Disease," Texas Heart Institute Heart Information Center, www.texasheartinstitute.org
4. Gijsen, F.J.H., van de Vosse, F.N., and Janssen, J.D., 1999, "The Influence of the Non-Newtonian Properties of Blood on the Flow in Large Arteries: Steady Flow in a Carotid Bifurcation Model," Journal of Biomechanics, Vol. 32, pp. 601-608.
5. Jou, L.D., and Berger, S.A., 1998, "Numerical Simulation of the Flow in the Carotid Bifurcation," Theoretical and Computational Fluid Dynamics, Vol. 10, pp. 239-248.
6. Perktold, K., Thurner, E., and Kenner, T., 1994, "Flow and Stress Characteristics in Rigid Walled and Compliant Carotid Artery Bifurcation Models," Medical and Biological Engineering and Computing," Vol. 32, pp. 19-26.
7. Perktold, K., and Rappitsch, G., 1995, "Computer Simulation of Local Blood Flow and Vessel Mechanics in a Compliant Carotid Artery Bifurcation Model," Journal of Biomechanics, Vol. 28, pp. 845-856.
8. Schneider, M., 2002, "Stroke Busters in Turbulent Blood," Pittsburgh Supercomputing Center Annual Research Report.
9. Stroud, J.S., Berger, S.A., and Saloner, D., 2002, "Numerical Analysis of Flow through a Severely Stenotic Carotid Artery Bifurcation," Journal of Biomechanical Engineering, Vol. 124, pp. 9-20.
10. Tang, D., Yang, C., Yuan, C., 2007, "Mechanical image analysis using finite element method," Carotid Disease, Cambridge University Press, pp. 324-340.
11. Younis, H.F., Kaazempur-Mofrad, M.R., Chan, R.C., Isasi, A.G., Hinton, D.P., Chau, A.H., Kim, L.A., Kamm, R.D., 2004, "Hemodynamics and wall mechanics in human carotd bifurcation and its consequences for atherogenesis: investigation of inter-individual variation," Biomechan Model Mechanobiol, Vol. 3, pp. 17-32.
12. S.Z., Zhao, X.Y., Xu, A.D., Hughes, S.A., Thom, A.V., Stanton, B., Ariff, Q., Long, 2000, "Blood flow and vessel mechanics in a physiologically realistic model of a human carotid arterial bifurcation," Journal of Biomechanics, Vol. 33, pp. 975-984.

SCOTT LOVALD
Scott Lovald received a BSME, MEME, and MBA from the University of New Mexico. Scott has been the recipient of a number of awards and research fellowships focused in the design and analysis of medical implants using the finite element method and computational fluid dynamics. Over the past five years, he has been involved in a number of projects and publications pertaining to craniomaxillofacial implant design including working with Stryker-Leibinger in Freiburg, Germany. Scott is currently pursuing a PhD in Mechanical Engineering at the University of New Mexico.

TARIQ KHRAISHI
Dr. Khraishi currently serves as an Associate Professor of Mechanical Engineering at the University of New Mexico. His general research interests are in theoretical, computational and experimental solid mechanics and materials science. He has taught classes in Dynamics, Materials Science, Advanced Mechanics of Materials, Elasticity and Numerical Methods. For the last four years he has engaged himself in the scholarship of teaching and learning."

JUAN HEINRICH
Dr. Heinrich received his undergraduate degree from Universidad Católica de Chile and his Ph.D. in Mathematics/Numerical Analysis from the University of Pittsburgh. He is currently editor, advisor and reviewer for a variety of technical journals, including *International Journal for Numerical Methods in Fluids* and *Progress in Computational Fluid Dynamics*. Juan started his academic career as a Professor at

the University of Arizona, and is currently Chairman of the Department of Mechanical Engineering at the University of New Mexico. He is co-author of the books *The Finite Element Method:Basic Concepts and Applications,* and *Intermediate Finite Element Method. Fluid Flow and Heat Transfer Applications,* with D. W. Pepper.

HOWARD YONAS
Dr. Yonas is the chairman of the Department of Neurosurgery. He obtained his undergraduate degree from the University of Pittsburgh and his MD degree from Ohio State University. Dr. Yonas is actively involved in developing new technologies for improving our understanding as well as the treatment of Cerebrovascular and traumatic disorders of the brain. Dr. Yonas helped develop and implement the use of quantitative cerebral blood flow measurements using the combination of stable xenon inhalation and CT scanning. He has authored over 180 articles and edited two books. Dr. Yonas is actively involved in studies designed to improve our understanding of traumatic as well as Cerebrovascular disorders.

CHRISTOPHER TAYLOR
Dr. Taylor is an Assistant Professor of Neurosurgery with a joint appointment in the Departments of Neurosurgery and Radiology. Dr. Taylor received his undergraduate degree from Eastern Mennonite College in Harrisonburg, Virginia and his medical degree from Case Western Reserve University in Cleveland, Ohio. His clinical interests include surgical and endovascular treatment of brain aneurysm, vascular malformation, and carotid artery disease. Dr. Taylor has published peer-reviewed articles and book chapters on topics including the epidemiology of subarachnoid hemorrhage, surgical and endovascular management of brain aneurysm, the acute management of stroke and others.